

<https://doi.org/10.1038/s42005-022-01010-1>

OPEN

## Quantum spin liquid candidate as superior refrigerant in cascade demagnetization cooling

Xin-Yang Liu<sup>1,2,8</sup>, Yuan Gao<sup>1,2,8</sup>, Han Li<sup>1,3</sup>, Wentao Jin<sup>1</sup>, Junsen Xiang<sup>4</sup>, Hai Jin<sup>5</sup>, Ziyu Chen<sup>1</sup>, Wei Li<sup>1,2,6,7✉</sup> & Gang Su<sup>1,3,6✉</sup>

The quantum spin liquid (QSL) states with no long-range magnetic order even down to zero temperature have recently raised intensive research interest. Here we propose that the spin frustration characteristic of the QSL candidates also make them superior magnetocaloric materials that exhibit prominent cooling effect, especially near the quantum critical points. By simulating the highly frustrated kagome and triangular lattice models, we reveal a significant magnetothermal pumping effect when combining quantum magnets with paramagnetic salts, which can be exploited to design a high-performance cascade demagnetization refrigerator. Moreover, with realistic magnetic compounds  $\text{YbAlO}_3$  and  $\text{Na}_2\text{BaCo}(\text{PO}_4)_2$ , we find a giant enhancement in the cooling capacity characterized by a great increment rate, e.g., more than 200% when working between 3 K heat sink and 30 mK load. Our work thus paves a promising and viable way for the quantum spin cooling to promote the helium-free refrigeration useful in space applications and quantum technologies.

<sup>1</sup>School of Physics, Beihang University, 100191 Beijing, China. <sup>2</sup>CAS Key Laboratory of Theoretical Physics, Institute of Theoretical Physics, Chinese Academy of Sciences, 100190 Beijing, China. <sup>3</sup>Kavli Institute for Theoretical Sciences, University of Chinese Academy of Sciences, 100190 Beijing, China. <sup>4</sup>Beijing National Laboratory for Condensed Matter Physics, Institute of Physics, Chinese Academy of Sciences, 100190 Beijing, China. <sup>5</sup>Department of Astronomy, Tsinghua Center for Astrophysics, Tsinghua University, 100084 Beijing, China. <sup>6</sup>CAS Center of Excellence in Topological Quantum Computation, University of Chinese Academy of Sciences, 100190 Beijing, China. <sup>7</sup>Peng Huanwu Collaborative Center for Research and Education, Beihang University, Beijing, China. <sup>8</sup>These authors contributed equally: Xin-Yang Liu, Yuan Gao. ✉email: [w.li@itp.ac.cn](mailto:w.li@itp.ac.cn); [gsu@ucas.ac.cn](mailto:gsu@ucas.ac.cn)

Magnetic materials can experience significant temperature changes when exposing to external magnetic fields, called magnetocaloric effect (MCE)<sup>1</sup>, which can be exploited to realize low-temperature cooling through the adiabatic demagnetization refrigeration (ADR)<sup>2,3</sup>. Nearly 90 years after the first realization of sub-Kelvin magnetic cooling<sup>3</sup>, the practical and commercial ADR refrigerators are still mostly using hydrate paramagnetic salts (see a brief introduction to conventional ADR in “Methods”). On the other hand, magnetic cooling becomes increasingly important due to the intensive use in space applications<sup>4–8</sup>, and potentially also in quantum computations<sup>9</sup> due to the global helium shortage. In practice, to accommodate the higher base temperature (say, a few Kelvins), lower working temperature (below 100 mK), and the required larger cooling power, it is highly desirable to seek for superior magnetocaloric materials with prominent MCE properties.

Given the swift progresses in the frustrated quantum magnetism studies, one promising direction is to extend the coolants from common paramagnetic salts to novel types of quantum magnets, and to design accordingly demagnetization refrigeration process. In ADR salts, spins are nearly non-interacting and quite dilute (i.e., spin-gas systems). This puts a strong constraint on their volumetric cooling power as well as the thermal conductivity at low temperature. However, when the spins are organized closer in the compounds, the spin interactions become stronger, and the magnet tends to order and loses the cooling power at a higher temperature. One intriguing exception is the highly frustrated quantum spin liquid (QSL) candidate<sup>10–12</sup>. Despite the relatively large spin densities and competing spin interactions, these highly frustrated magnets do not order even in the ground state due to strong quantum fluctuations. In particular, for the gapless QSL systems there possess anomalously large entropies till very low temperatures, and when the QSL candidate materials are driven towards the quantum critical points (QCPs)<sup>13</sup>, they can exhibit pronounced MCE response in the low-temperature quantum critical regime.

In this work, we propose the QSL candidate materials, whose number is rapidly increasing, can offer superior quantum magnet coolants with giant MCE. We simulate with several highly frustrated QSL models, and observe pronounced MCE near the QCP, dubbed as quantum critical refrigeration (QCR)<sup>14–29</sup> that is complementary to conventional ADR. By combining the QCR and ADR coolants, we find a large entropy pumping between the two in a demagnetization process, which can be exploited to boost the magnetic cooling. Importantly, there exist realistic low-dimensional materials that can serve as quantum spin coolants. We consider the 1D Tomonaga–Luttinger liquid (TLL) material YbAlO<sub>3</sub> (YAO)<sup>30</sup> and the triangular-lattice QSL candidate Na<sub>2</sub>BaCo(PO<sub>4</sub>)<sub>2</sub> (NBCP)<sup>31–34</sup>, and show—based on experimental thermal data of the two compounds—that they indeed constitute superior refrigerants with pronounced MCE performance.

## Results

**Frustrated spin models and quantum critical MCE.** The frustrated magnets exhibit strong MCE in the quantum critical regime. This can be seen by simulating the finite-temperature properties of Heisenberg spin models defined on the kagome (KLH) and triangular (TLH) lattices shown in Fig. 1a, which is compared to the square lattice Heisenberg (SLH) model. The Heisenberg model is in general defined as

$$H = \sum_{\langle i,j \rangle} J \mathbf{S}_i \cdot \mathbf{S}_j + \sum_{\langle\langle i,j \rangle\rangle} J' \mathbf{S}_i \cdot \mathbf{S}_j - B \sum_i g \mu_B S_i^z, \quad (1)$$

with antiferromagnetic  $J$  and  $J'$  spin couplings between nearest (NN) and next-nearest neighboring (NNN) sites.

Below we consider the highly frustrated TLH model with both NN and NNN interactions with a ratio  $J'/J = 0.1$ , thus in the putative QSL regime<sup>35–38</sup>. Besides, the KLH is also believed to host a QSL ground state<sup>39–43</sup>. For the Heisenberg models, there always exists a QCP at the field  $B = B_c$  where the spins become fully polarized, due to the presence of spin rotational U(1) symmetry. The polarization field can be determined accurately with the semi-classical analysis and confirmed by the density matrix renormalization group calculations (see “Methods”). With the state-of-the-art thermal tensor network approach<sup>44–47</sup>, we can accurately compute the thermodynamic quantities down to very low temperatures and explore the significant MCE of various frustrated and unfrustrated models. In practice, there are also lattice contributions (and even nuclear spin contributions) in realistic magnetic material<sup>48</sup>, which play an essential role to achieve thermal equilibrium of the system. However, as the lattice phonon-specific heat is typically negligibly small in the sub-Kelvin regime, we regard the spins are in a nearly adiabatic condition and consider only the spin model in the analysis of magnetocaloric effects in the present work. To compare them on an equal footing, we fine-tune the coupling parameters in the spin models such that the polarization field is fixed as  $B_c = 1$  T in the simulations (Supplementary Table S2).

We start with certain highly frustrated QSL models and reveal their excellent MCE properties. In Fig. 1b, we compare the frustrated KLH and TLH models with the unfrustrated SLH model. The entropy curves of ADR salts can be computed with the entropy formula of paramagnets with empirical parameters (see “Methods”). From Fig. 1b, we see the SLH coolant exhibits enhanced MCE response near the critical field of 1 T and can reach a lower temperature  $T_M$  than that ( $T_{B_0}$ ) of the spin-1/2 ADR salt, when following the adiabatic line (horizontal dashed line in Fig. 1b). Moreover, the two frustrated QSL magnets, TLH and KLH, are found to exhibit even larger entropies near the QCP and can reach even lower  $T_M$ . As highlighted in Fig. 1b, a larger temperature drop  $\Delta T_M = T_{B_0} - T_M$  is thus observed for the frustrated models. This can be ascribed to the large density of low-lying excited states due to strong frustration effects<sup>21,22</sup>. Besides the huge temperature drop, in Fig. 1b we also observe a significant isothermal entropy change at very low temperature (e.g., 100 mK) as field ramps down from 4 T to 1 T. In contrast, the ADR salts show virtually zero entropy change under the same condition.

The different MCE properties of the QCR and ADR stages are also clearly reflected in their different magnetic Grüneisen parameter  $\Gamma_B = \frac{1}{T} \left( \frac{\partial T}{\partial B} \right)_S$  shown in the inset of Fig. 1d.  $\Gamma_B$  of the ADR salt exhibits a peak very close to the zero field that decreases rapidly when moving away from there, while  $\Gamma_B$  of the QCR coolant diverges near the QCP at a finite critical field  $B_c$ , responsible for the corresponding steep temperature drop.

In the analysis above, we compared the MCE responses between two frustrated QSL models and the unfrustrated SLH near the polarization transition  $B_c$ , and find the formers lead to the significantly more prominent cooling effect. Moreover, not limited to the regime near the polarization field  $B_c$ , the QSL systems also exhibit strong cooling effects continuously and persistently in the regime  $B \leq B_c$ , in sharp distinction to the unfrustrated spin ordered systems (see details in “Methods”). This can be ascribed to the strong variations of the magnetization versus temperatures and/or fields due to strongly competing spin orders below the polarization field<sup>49</sup>. Nevertheless, for the sake of discussion, we focus henceforth on the enhanced MCE near  $B_c$  and discuss its implication in high-performance magnetic cooling.

**Magnetothermal pumping and the cascade-demagnetization cooling.** To fully exploit the cooling ability of QCR coolants at the

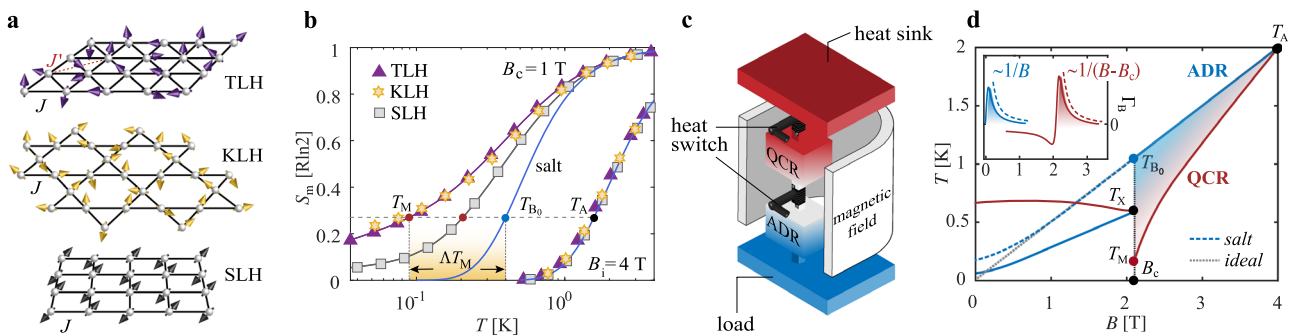


**Fig. 1 Spin lattice models, magnetothermal entropy pumping, and cascade demagnetization.** **a** shows various quantum spin models including the triangular-lattice Heisenberg (TLH) with both nearest ( $J$ ) and next-nearest ( $J'$ ) spin couplings, kagome lattice Heisenberg (KLH), and the square lattice Heisenberg (SLH) models. **b** shows the magnetic entropies  $S_m$  (in unit of  $R \ln 2$ , with  $R$  the ideal gas constant) at a high magnetic field of  $B_i = 4$  T and the transition field  $B_c = 1$  T. The entropy curves of a spin-1/2 adiabatic demagnetization refrigeration (ADR) salt  $\text{Ce}_2\text{Mg}_3(\text{No}_3)_{12} \cdot 24\text{H}_2\text{O}$  (CMN) are also plotted as a comparison.  $T_{B_0}$  and  $T_M$  represent the reached low temperatures through the same adiabatic demagnetization process (illustrated by the dashed horizontal line starting from  $T_A \equiv T_i$ ) of the ADR and quantum critical refrigeration (QCR) coolants, respectively.  $\Delta T_M$  denotes the additional temperature drop of the ADR stage due to the magnetothermal pumping of QCR. **c** shows the proposal of multi-stage cascade refrigeration that combines the (upper) QCR and (lower) ADR stages through a heat switch, with both stages connected to the heat sink via another switch. The refrigerator works between a high-temperature heat sink of 3–4 K and a low-temperature load below 100 mK, enclosed by a superconducting magnet with a peak field of 4 T. The refrigeration mechanism is illustrated in **d**. As the magnetic field ramps down, the QCR decreases the temperature rapidly near  $B_c$  and reaches  $T_M$  much lower than  $T_{B_0}$ , and it thus cools down the conventional ADR salts to an intermediate temperature  $T_X$  (for two coolants in stoichiometrically 1:1 ratio) or even  $T_M$  (when QCR coolants dominate) as the thermal switch between the two stages is closed (i.e., thermally connected). This enables the ADR to achieve a lower temperature in the continued ADR process with additional cooling capacity gained. Meanwhile, the QCR stage follows the red solid line and serves as an excellent thermal guard. **d** We also show the isentropic (blue dashed) line of the ADR salt that firstly follows the ideal (gray dotted) line with constant  $T/B$  and eventually deviates from it at certain low temperature. The inset shows the schematic plot of the magnetic Grüneisen parameter  $\Gamma_B$  of the ADR and QCR coolants, where the ADR(QCR) coolant has a divergent  $\Gamma_B$  peak near zero(finite) field. The dashed lines indicate their asymptotic divergence scalings at sufficiently low temperatures.

transition field  $B_c$  and that of ADR salts near zero field, we propose multi-stage cascading refrigeration that properly combine the two types of coolants. This is based on the following observation: a significant amount of entropies can be pumped out of the ADR stage into the QCR stage, when both are under a common field in the demagnetization process and in a thermal contact. As shown in Fig. 1b, such a large entropy pumping helps the ADR stage to reach lower working temperature and gain greatly enhanced cooling capacity.

The model of cascade refrigerator is shown in Fig. 1c, which consists of two stages, namely, the QCR and ADR stages. The working illustrated is explained in Fig. 1d. As the field ramps down from the peak field  $B_i$ , the temperatures of both stages decrease, and the QCR stage cools down significantly faster than the ADR coolants. To be concrete, the QCR isentropic ( $T$ - $B$ ) line exhibits a distinct dip near the QCP at  $B_c$ , and thus attains a considerably lower temperature ( $T_M$ ) than that ( $T_{B_0}$ ) of the ADR. Therefore, by keeping the two stages in thermal contact for  $B \geq B_c$ , heat/entropy will be pumped from the lower ADR to the upper QCR stage. Below  $B_c$ , the heat switch is opened (and thus no thermal contact), and the ADR salt reaches the low working temperature  $T_w$  as the field further ramps down. In the successive hold process, the ADR stage provides high cooling power, while the upper QCR stage is not temperature controlled. Instead, it constitutes an excellent thermal guard absorbing the parasitic heat (see more details on the cascade-demagnetization circulation in Supplementary Note 1 with Supplementary Fig. S1 and Supplementary Table S1).

Such a cascade design fully takes the advantages of the QCR and ADR refrigerants of complementary MCE properties, and achieves an overall great improvement in the cooling performance. Comparing our design in Fig. 1c to the widely used Hagmann–Richards (HR) refrigerator<sup>4,8</sup>, the subtle yet crucial difference is to allow the upper and lower stages to exchange heat in the first period of the demagnetization cooling ( $B \geq B_c$ ).

In contrast, there exists no such thermal contact between the two stages in the HR design, where the upper stage thus serves merely as a thermal guard. Moreover, it is worthwhile to point out, even if there were thermal contact allowed between the two ADR stages, there would be no magnetothermal pumping between the two paramagnetic salts and thus no gain in cooling capacity like in the QCR-ADR combination. As shown in Fig. 1d, since the magnetic entropies of the ideal paramagnetic salt only depend on the ratio  $T/B$ , all ADR salts starting from the same base temperature ( $T_i$ ) and peak magnetic field ( $B_i$ ) should follow a common straight  $T$ - $B$  line (of constant slope  $T_i/B_i$ ) and always reach the same temperature under the same field in the course of demagnetization process (see more discussions in Supplementary Note 2). This is in sharp contrast to our cascade design combining the QCR and ADR coolants with essentially different MCE properties.

**Boosted cooling capacity.** The cascade cooling process with QCR and ADR coolants can lead to a boost in the overall cooling capacity. In Fig. 2a, we plot the entropy curves of the ADR salt (CMN) and QCR coolant modeled by Heisenberg anti-ferromagnetic chain (HAFC, a 1D spin liquid), both of which are of spin  $S = 1/2$  and have the same saturation entropy  $R \ln 2$  per mole. Though CMN can reach a remarkably low temperature (1.5 mK), its cooling capacity is rather limited when working with a relatively high-temperature heat sink ( $T_i$ )—exactly the issue we would like to address here.

When we consider combining the QCR and ADR coolants in a cooling circle, there are two cases that we focus on henceforth and will be frequently referred to. When the QCR and ADR coolants are in a stoichiometrically 1:1 combination (i.e., the same mole of spins, dubbed X mode), the average entropy is  $S_{\text{mean}}(T) = \frac{1}{2}[S_{\text{QCR}}(T) + S_{\text{ADR}}(T)]$  as indicated by the red dashed red lines in Fig. 2a. On the other hand, note that the QCR coolants as

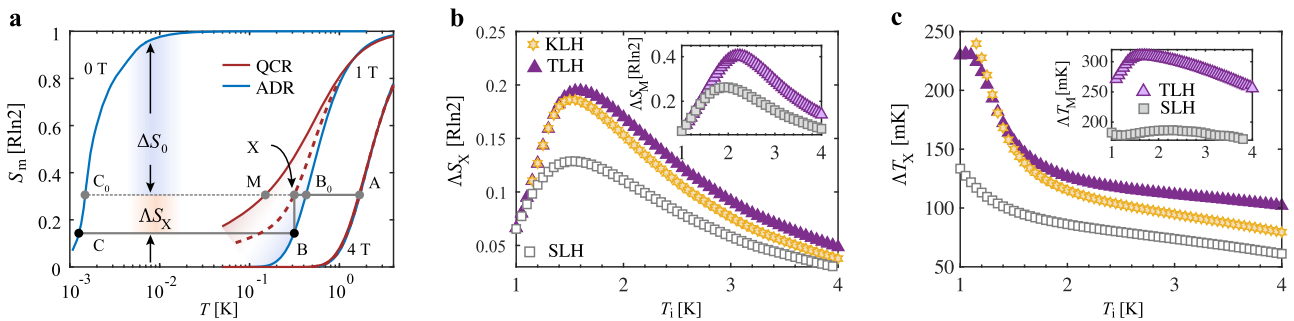


**Fig. 2 Magnetocaloric effect enhancement in cascade cooling.** **a** shows the entropy curves of the quantum critical refrigeration (QCR) coolant (simulated by the Heisenberg antiferromagnetic chain model) and the adiabatic demagnetization refrigeration (ADR) salt ( $\text{Ce}_2\text{Mg}_3(\text{NO}_3)_{12} \cdot 24\text{H}_2\text{O}$ , CMN) under various fields including the peak value  $B_i = 4\text{ T}$ , the critical value  $B_c = 1\text{ T}$  of QCR, and the zero field (for CMN only). The red dashed curves represent the mean entropies of QCR and ADR at  $B_i = 4\text{ T}$  and  $B_c = 1\text{ T}$ .  $\Delta S_0$  means the entropy change of a bare CMN stage (or the lower stage in the HR refrigerator, to be more precise), and the enhancement  $\Delta S_X$  in the QCR-ADR cascading is also highlighted. In the cascade design, CMN stage follows the staircase-like A-X(M)-B-C path in the demagnetization process, in contrast to the original A- $B_0$ - $C_0$  one. As entropy  $\Delta S_X$  is pumped from the ADR to the QCR stage as the field ramps down from  $B_i$  to  $B_c$ , the former gets extra cooling capacity. **b** collects the enhancements, i.e., pumped entropies  $\Delta S_X$  and  $\Delta S_M$  (in the inset), due to QCR stages modeled by three spin lattice models. The additional temperature decrease  $\Delta T_X$  (main panel) and  $\Delta T_M$  (inset) are shown in **c**, versus various base temperature  $T_i$ .

correlated magnets have generically much larger spin density than those of the (paramagnetic) ADR salts, therefore we also consider the case that  $S_{\text{mean}}(T) \approx S_{\text{QCR}}(T)$  (following the red solid line in Fig. 2a, dubbed M mode). This case happens when the two coolants are in a more or less isovolumetric combination.

In the QCR-ADR cascade refrigeration, we characterize the cooling capacity enhancement by the entropy change at a low working temperature, as indicated by the vertical arrow in Fig. 2a. Without the QCR stage, the salt CMN follows the A- $B_0$ - $C_0$  line and can absorb  $\Delta S_0$  entropy from the heat load at low working temperature. On the other hand in the QCR-ADR cascade system, it starts from the A point, where the entropy curves of the QCR and ADR coolants virtually coincide at a high field of  $B_i = 4\text{ T}$ . In the demagnetization procedure, the system adiabatically moves to the point X or M and a huge amount of entropies (denoted as  $\Delta S_X$  or  $\Delta S_M$ ) are pumped from the salt ADR to the QCR stages, which are turned eventually into the enhanced cooling capacity.

Moreover, we collect the enhanced entropy changes  $\Delta S$  and plot them in Fig. 2b versus various base (heat sink) temperatures  $T_i$ . The two highly frustrated QSL model coolants TLH and KLH exhibit much stronger enhancement over the unfrustrated SLH: the TLH has overall largest entropy pumping  $\Delta S_X \simeq 0.2 R \ln 2$  (with  $T_i \simeq 1.6\text{ K}$ , main panel) and  $\Delta S_M \simeq 0.4 R \ln 2$  (with  $T_i \simeq 2.2\text{ K}$ , the inset), clearly greater than those of the SLH coolant.

In Fig. 2c, we show the enhancements in adiabatic temperature change at  $B_c$ , including  $\Delta T_X = T_{B_0} - T_X$  and  $\Delta T_M = T_{B_0} - T_M$ . The frustrated coolants are again found to result in a significantly larger temperature drop than that of the unfrustrated SLH. In Fig. 2c, the TLH coolant leads to a particularly strong cooling effect with  $\Delta T_X \simeq 126\text{ mK}$  and  $\Delta T_M \simeq 307\text{ mK}$  (for  $T_i = 2\text{ K}$ ). Remember the ADR salts under the same condition is cooled down to  $T_{B_0} \simeq 500\text{ mK}$ , and thus the relative temperature drop are very prominent as  $\delta_{\Delta T}^X = \Delta T_X/T_{B_0} \simeq 25.2\%$  and  $\delta_{\Delta T}^M = \Delta T_M/T_{B_0} \simeq 61.4\%$ , respectively. Such a strong MCE can be related to the anomalous low-temperature thermodynamics<sup>50,51</sup> due to the strong spin frustration and roton-like excitations, and become particularly strong when a moderate NNN coupling  $J' > 0$  is present<sup>52</sup>.

**Realistic QSL candidates as quantum material coolants.** Based on the spin model studies above, we find the frustrated spin models on the kagome and triangular lattices serve as excellent QCR coolants that can greatly enhance the cooling capacity via

the proposed QCR-ADR cascade refrigeration. Relevant for experiments, our conclusion renders a useful guide for searching superior sub-Kelvin refrigerants in the QSL candidate materials. Now we turn to two realistic magnetic materials, a triangular-lattice QSL candidate NBCP and a rare-earth spin-chain compound YAO, both of which are spin-orbit magnets with effective spin  $S = 1/2$ . From experiments, they are found to have only moderate critical fields, i.e.,  $B_c \simeq 1.1\text{ T}$  for YAO and around  $1\text{ T}$  for NBCP. Moreover, YAO is shown to possess a 1D TLL state with multi-spinon continuum excitations<sup>30</sup>, and in NBCP there are strong low-energy fluctuations that are currently under active investigations<sup>31-34</sup>. Below we consider cascading these realistic magnetic compounds with the ADR salts including CMN and  $\text{CrK}(\text{SO}_4)_2 \cdot 12\text{H}_2\text{O}$  (CPA). The CPA, albeit with an ordering temperature a bit higher (10 mK) than that of CMN, is commonly used in practical refrigeration due to the relatively high cooling power as Cr ion carries a larger spin of  $S = 3/2$ <sup>6,9</sup>.

In Fig. 3a, d, we show respectively the entropy curves of YAO and NBCP, with the pumped entropy  $\Delta S_M$  clearly indicated, which are then collected and plotted versus various base temperatures  $T_i$  in Fig. 3b, e. The QSL candidate NBCP and TLL compound YAO can lead to a similar maximal entropy pumping  $\Delta S_M \simeq 0.8 R \ln 2$  that is remarkably large. Furthermore, in Fig. 3c, f, we show the relative cooling capacity enhancement  $\delta_{\Delta S}^M(T_w) = \Delta S_M/\Delta S_0(T_w)$  increases as the working temperature  $T_w$  lowers. This is since the entropy change  $\Delta S_0$  of the ADR salt decreases rapidly near the Schottky anomaly (Supplementary Fig. S2), while the enhancement  $\Delta S_M$  is a constant regardless of any specific working temperature  $T_w$ . Taking the NBCP-CPA cascade as an example, we find  $\Delta S_M \simeq 0.65 R \ln 2$  (from the base temperature  $T_i = 3\text{ K}$ , c.f., Fig. 3e) that leads to an increase rate over 400% near  $T_w = 20\text{ mK}$  (c.f., Fig. 3f). In Fig. 3, we show the maximal enhancement (in the M mode) and leave the stoichiometrically 1:1 combination in the Supplementary Note 3. Overall, the QSL model simulations in Fig. 2 and realistic materials analysis in Fig. 3 demonstrate clearly the great potential of quantum material cooling using low-dimensional quantum magnets and in particular QSL candidates with strong spin frustration.

**Cooling performance characteristics.** The cooling capacity and related hold time (duration of the hold process, see “Methods”) constitute important parameters characterizing the practical MCE performances. In Table 1 we compare the MCE performances of

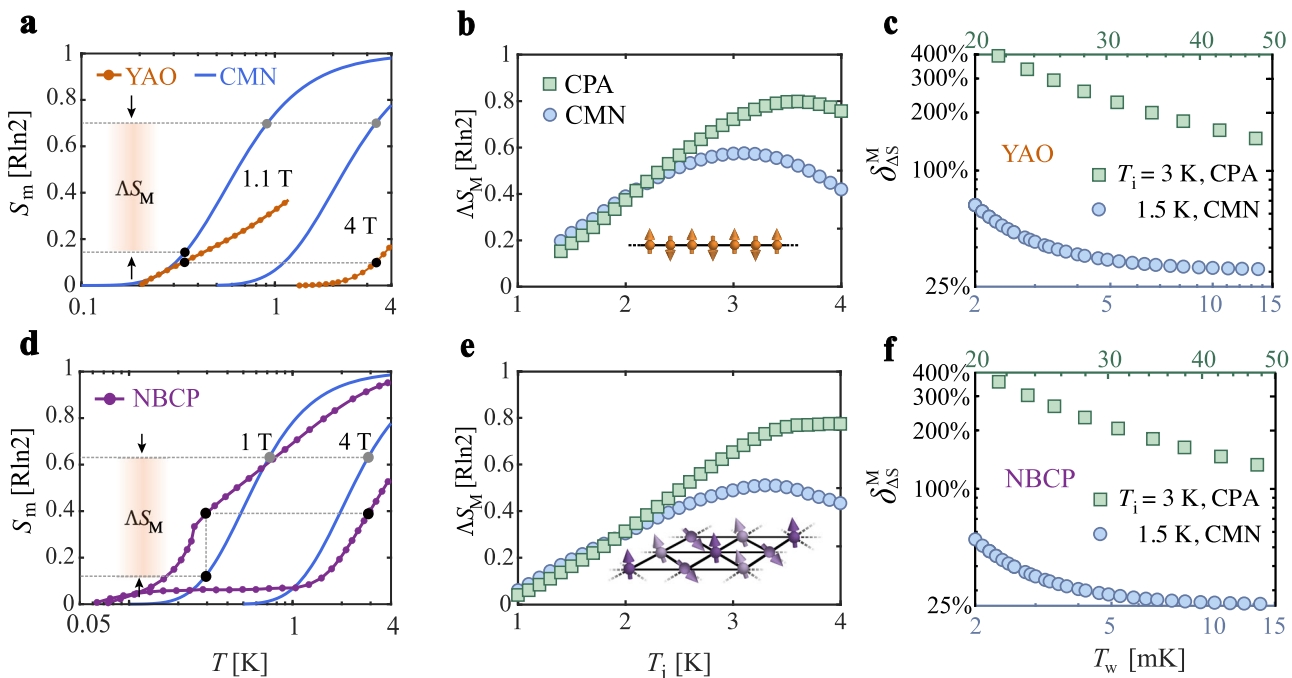


**Fig. 3 Giant enhancement in magnetocaloric effect with two spin-liquid coolants  $\text{YbAlO}_3$  (YAO) and  $\text{Na}_2\text{BaCo}(\text{PO}_4)_2$  (NBCP).** **a, d** show the entropy curves of YAO and NBCP, as well as the ADR salt  $\text{Ce}_2\text{Mg}_3(\text{NO}_3)_{12} \cdot 24\text{H}_2\text{O}$  (CMN), under the peak field  $B_i = 4\text{ T}$  and the critical field around  $1\text{ T}$ , respectively. The entropy change enhancement  $\Delta S_M$  is also indicated. **b, e** We show  $\Delta S_M$  of salts CMN and  $\text{CrK}(\text{SO}_4)_2 \cdot 12\text{H}_2\text{O}$ , due to the combination with the spin-liquid coolants YAO and NBCP, at various base temperature  $T_i$ . The insets illustrate the spin-chain and triangular-lattice structures for both YAO and NBCP compounds. **c, f** show, respectively, the increment rates of two spin-liquid coolants at various working temperatures  $T_w$ , when combined with CMN (from base  $T_i = 1.5\text{ K}$ ) and CPA ( $T_i = 3\text{ K}$ ).

conventional ADR (in a HR refrigerator) and our QCR-ADR cascade cooling. The sizable increase in entropy change shown in Fig. 3 corresponds to large cooling capacities ( $A_0 = \Delta S_0 \cdot T_w$  and  $A_h = (\Delta S_0 + \Delta S_{X,M}) \cdot T_w$ , in unit of  $\mu\text{W} \cdot \text{h/mol}$ ) and the long hold time (h/mol). From Table 1, we find for the NBCP-CPA combination with similar masses (X mode) the hold time can be enhanced from 21.05 h (per mol coolant) to 28 h, i.e., increased by 33.3%, when working between the heat sink  $T_i = 3\text{ K}$  and load  $T_w = 50\text{ mK}$ . On the other hand, in the M mode that the QCR coolants dominate in mole, the hold time further increases to 47.2 h, i.e., by about 124%. Besides, in Table 1 we have also listed the cases down to even lower working temperatures, where we find an enormous increment rate more than 215%, with the hold time expanded from 8.05 h/mol to 25.4 h/mol when working between 3 K heat sink and 30 mK load. Besides, to reach even lower working temperature  $T_w = 15\text{ mK}$  (from the base temperature  $T_i = 1.5\text{ K}$ ) the hold time can be extended up to 25% in the NBCP-CMN combination.

Besides the cooling capacity and hold time increment, it is also important to check the sample temperature  $T_s$  of the QCR coolants in the upper stage. This is important since the temperature of the heat sink is, as shown in Table 1, 30–100 times of the working temperature  $T_w \leq 50\text{ mK}$ , which spans a too wide temperature range and the cooling system thus suffers from large parasitic heat loads. Now in the cascade refrigerator, the upper QCR stage cools down to an intermediate temperature (c.f.,  $T_X$  and  $T_M$  in Table 1), which is now only about 5–15 times of  $T_w$  and can ideally serve as a thermal guard to reduce the parasitic heat. Accordingly, we need the sample temperatures to be stable in the hold process. To check that, we have also calculated the sample temperature under a constant heat load of  $5\text{ }\mu\text{W}$ , and found both the YAO and NBCP can hold below 1 K for sufficiently long hours (more than 50 h, from the 500 mK base

temperature and per mole coolants), providing excellent protection of the lower ADR stage from the high-temperature heat sink (see Supplementary Note 3).

Moreover, we point out the efficiency of the cascade refrigeration is also higher than the traditional ADR (e.g., in a HR refrigerator). The high-efficiency  $\eta = \Delta Q_a / \Delta Q_r$  (with  $\Delta Q_a$  ( $\Delta Q_r$ ) the absorbed (repealed) heat in a circulation) of the quantum spin coolants has been noticed before in a different context<sup>15,16</sup>, which can be ascribed to the large specific heat of the quantum magnet. Here we note the lower ADR stage also has an enhanced efficiency  $\eta$  in the cascade design. As it absorbs heat at the low working temperature  $T_w$ , while repeals heat to the sink and upper stage at  $T_i$  and  $T_{X,M}$ , respectively, thus  $\eta$  should be greater than  $T_w/T_i$  —the highest possible efficiency of the conventional ADR cooling.

## Discussion

In different field ranges, the QCR and ADR coolants have prominent MCE properties characterized by the diverging Grüneisen parameters. Therefore, by combining the two kinds of refrigerants, we design a cascade refrigeration that boosts the cooling capacity by exploiting the strong magnetothermal pumping between the two stages. We examine the proposal with simulations of the highly frustrated QSL models and identify the great advantage with two realistic compounds, i.e., the TLL material YAO and QSL candidate NBCP. With this cascade refrigeration framework proposed, the quantum material coolants are ready to play their active roles in the sub-Kelvin magnetic refrigeration. Note the strong spin frustration and low dimensionality, as essential ingredients in searching promising QSL candidate materials, now also constitute key factors for finding superior magnetocaloric materials.

**Table 1 Comparisons of the cooling capacity and hold time of various adiabatic demagnetization refrigeration (ADR) salts with and without the quantum critical refrigeration (QCR) stage.**

Temperatures		Conventional ADR			QCR/ADR cascade refrigeration						
$T_i$ (K)	$T_w$ (mK)	$A_0$ ( $\mu\text{W} \cdot \text{h/mol}$ )	$t_0$ (h/mol)	Coolant	$T_x$ (mK)	$T_m$ (mK)	$A_h$	$t_h$	$\delta_A^X$	$\delta_A^M$	Coolants
3	50	42.1	21.05	CPA	647.9	283.9	54.4-98.0	27.2-49	29.8%	132.8%	YAO-CPA
3	50	42.1	21.05	CPA	634.3	324	56.1-94.4	28-47.2	33.3%	124.2%	NBCP-CPA
3	30	16.1	8.05	CPA	634.3	324	24.3-50.8	12.1-25.4	50.8%	215.4%	NBCP-CPA
1.5	15	18.4	9.2	CMN	291	223.9	21.3	-23.0	10.6-11.5	25.0%	NBCP-CMN

The characteristics of the conventional ADR refrigerator and in the proposed QCR-ADR cascade refrigerator are listed and compared. The ADR and QCR coolants are indicated in corresponding rows. The estimated  $t_0$  represents the hold time using  $\text{Cr}(\text{SO}_4)_2 \cdot 12\text{H}_2\text{O}$  (CPA) or  $\text{Ce}_2\text{Mg}_3(\text{NO}_3)_2 \cdot 24\text{H}_2\text{O}$  (CMN) in the upper stage. Depending on X mode (corresponding to the temperature  $T_x$ ) or the M mode ( $T_m$ ), the enhanced  $A_h$  (and  $t_h$ ) can span a finite range, with the corresponding increased ratios  $\delta_A^X \equiv \delta_{\Delta S}^X$  and  $\delta_A^M \equiv \delta_{\Delta S}^M$  also indicated. They measure the relative enhancement in the cooling capacity  $A_h$  (and also the hold time  $t_h$ ) in the QCR-ADR cascade refrigeration. In the calculations, we assume a peak field of 4 T and a heat load of 2  $\mu\text{W}$ .

To be specific, our proposal makes use of cutting-edge quantum material studies to facilitate helium-free refrigeration down to deep sub-Kelvin regime, which is useful in a number of aspects. First, the cascade refrigerator can greatly enhance the cooling capacity below 100 mK that are very important for space applications. When using CMN as the lower stage, a large cooling capacity enhancement is observed even below 10 mK (see Fig. 3c, f). This will be useful for quantum computers working in such a low-temperature regime. Moreover, when combined with a successive nuclear ADR stage, our NBCP-CMN cascade refrigeration can also help to reach temperatures below 1 mK since the nuclear ADR usually starts from a base temperature of about 10–20 mK. Overall, harnessing the power of frustrated quantum materials, our design can work across a wide temperature range with a reduced number of superconducting magnets, providing a compact and highly efficient design of the refrigerator with reduced mass and volume.

As guiding lines for experimentalists to find such quantum material refrigerants with high cooling performance, we point out that they are more likely to be found in magnetic materials with low spatial dimensionality and strong spin frustrations. Specifically, the suitable quantum magnet coolants better satisfy the following conditions: (i) the magnet does not order till extremely low temperature; (ii) it has strong spin fluctuations and (thus) large magnetic entropies at low temperature; and (iii) there exists a field-driven QCP at moderate fields. It can be immediately realized that, the conditions (i) and (ii) are naturally satisfied by the QSL candidate materials.

Swift progresses in recent studies of frustrated magnets offer a large number of potential spin-liquid coolants that also satisfy condition (iii). They are advantageous in several aspects: the spin densities in these compounds are usually much larger (typically  $10^{22} \text{ cm}^{-3}$ ) than those of the conventional ADR salts ( $\sim 10^{21} \text{ cm}^{-3}$ ). Secondly, the quantum magnets can have massive low-energy spin excitations, particularly near the QCP, that enables relatively large thermal conductivity profitable for exploiting their cooling powers. Lastly, thanks to the rich diversity of quantum magnetic material with various types of QCPs, it allows for flexible and versatile magnetic refrigeration designs. For instance, when the field drives a gapped quantum magnetic material to approach the QCP, a significant inverse MCE (iMCE) may appear at low temperature<sup>20,26</sup> that can be used to design an iMCE-ADR refrigeration, a compact continuous design that only requires a single superconducting magnet.

Some prominent examples of potential quantum material coolants include the triangular-lattice compound  $\text{REMgGaO}_4$  (RE = rare earth)<sup>53–62</sup>,  $\text{AYbSe}_2$  (A=Na, K, Rb)<sup>63–65</sup> and other chalcogenides<sup>66</sup>,  $\text{KBaRE}(\text{BO}_3)_2$ <sup>29,67</sup>, spin-orbit Kitaev materials  $\text{Na}_2\text{Co}_2\text{TeO}_6$ <sup>68,69</sup> and  $\text{BaCo}_2(\text{AsO}_4)_2$ <sup>70</sup>, rare-earth tripod kagome compound  $\text{Mg}_2\text{RE}_3\text{Sb}_3\text{O}_{14}$ <sup>71,72</sup>, etc. In Supplementary Note 4, we analyze the MCE properties of a quantum Ising magnet  $\text{TmMgGaO}_4$  based on the measured thermal data<sup>58,59,73</sup>. As this compound possesses a higher critical field of about 2.5 T,  $\text{TmMgGaO}_4$  could serve as a very nice option for cascade refrigeration with more than two stages to further enhance the cooling capacity. Actually, we expect the flexible design can exploit not only the Mott insulating magnetic materials discussed above, but also other systems like the heavy-electron metallic compounds<sup>19,28</sup>, turning their prominent MCE property to practical functionality.

Overall, with the merits of cascade-demagnetization cooling demonstrated and given the arsenal of frustrated quantum magnets of various types, our work opens the venue for quantum material cascade cooling, and calls for more experimental and theoretical studies of the magnetothermal properties of frustrated compounds and in particular the QSL candidate materials.

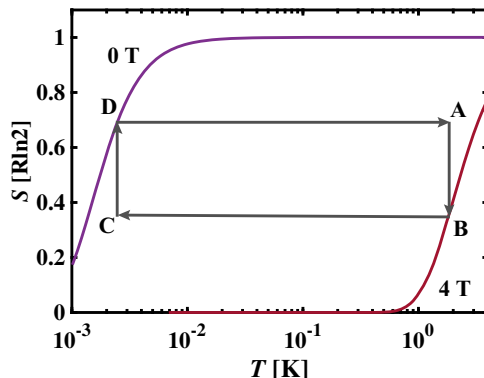


**Fig. 4 Conventional adiabatic demagnetization refrigeration (ADR) refrigeration circulation.**

**refrigeration circulation.** The one-shot adiabatic demagnetization refrigeration follows the A-B-C-D loop consisted of two adiabatic processes (B → C and D → A) and two isothermal processes (A → B and C → D). In the plot, the entropy curves of the paramagnetic salt are computed based on Eq. (2) with the  $\text{Ce}_2\text{Mg}_3(\text{NO}_3)_{12} \cdot 24\text{H}_2\text{O}$  parameters.

## Methods

**Conventional ADR and magnetic entropy of the paramagnetic salt.** Here we introduce the conventional, one-shot ADR refrigeration with the paramagnetic coolants<sup>6,74</sup>. In Fig. 4, we show the cooling circle, taking a  $S = 1/2$  paramagnetic salt (with the CMN parameters) as an example. We assume the peak field of 4 T and a heat sink temperature of 2 K. The circle starts from point A, and the field ramps up towards the maximal value of 4 T (B point) and expel heat to the reservoir. From point B, we open the heat switch and ramps down the magnetic field adiabatically from the peak value of 4 T. The salt cools down and reach the load temperature at point C. During the hold process (C → D), the field further ramps down and absorb heat from the load. Eventually, when the field reduces to zero (D), at which point the ADR's cooling capacity is exhausted. To restore the system, we increase the magnetic field adiabatically and bring the temperature to the heat sink temperature (A). The circulation can continue on and on as described above.

In the analysis of the cooling capacity of the conventional ADR and cascade refrigeration, the entropy curves of ADR salts, including CMN and CPA, etc., are very useful. The magnetic entropies of these salts can be calculated via the entropy formula

$$S_m/R = \chi \coth(\chi) - (2S+1)\chi \coth[(2S+1)\chi] + \ln[\sinh[(2S+1)\chi]/\sinh(\chi)], \quad (2)$$

where  $\chi = g\mu_B B_{\text{eff}}/2k_B T$  with  $\mu_B$  the Bohr magneton,  $k_B$  the Boltzmann constant,  $S$  the spin quantum number, and  $g$  the Landé factor. Here only spin entropies are considered as the phonon contributions are very small (e.g., refs. 15,53) and can be safely neglected in the analysis of sub-Kelvin cooling.

The effective field  $B_{\text{eff}} = \sqrt{B^2 + b(T)^2}$  relates to both external fields ( $B$ ) and residual spin-spin interaction [represented by  $b(T)$ ] in the ADR salts, with  $b(T) = b_0$  (for CMN, constant) and  $b(T) = b_0[1 - e^{-(T/T_0)^a}]$  (for CPA). The parameters  $b_0$ ,  $T_0$ , and  $a$  are empirical, which was obtained by fitting the experimental entropy data of the salts. To be specific, for CMN ( $S = 1/2$ ) it was found  $b = 0.003$  T, and for CPA ( $S = 3/2$ ) the parameters are  $b_0 = 0.0841$  T,  $T_0 = 0.0836$  K, and  $a = 0.7973$  (from ref. 8). These parameter sets generate entropy data in excellent agreement with the experiments (see Supplementary Fig. S2). The Schottky anomaly in the salts limits the lowest temperature ADR process can reach, e.g., 30 mK for  $\text{Fe}(\text{SO}_4)_2(\text{NH}_4)_2 \cdot 6\text{H}_2\text{O}$  (FAA, spin-5/2), 10 mK for CPA with spin-3/2, and 1.5 mK for the spin-1/2 CMN<sup>8</sup>. On the other hand, the entropy density of the refrigerants determine the maximal entropy (per volume) it can absorb from the heat load—the cooling capacity in the hold process (C → D in Fig. 4).

**Density matrix renormalization group.** We employ the density matrix renormalization group (DMRG) approach<sup>75–77</sup> to calculate the many-body ground states, e.g., the magnetization curves (at  $T = 0$ ) of various frustrated and unfrustrated spin models. The DMRG simulations are very accurate in the determination of the polarization field of the magnets defined on a finite-size system (in practice up to lattice geometry with width 6, see details in Supplementary Note 2). Since we only focus on the high field regime of the magnetization curve and the quantum entanglements are modest, we find a relatively small bond dimension  $D = 200–400$  already very well converges the results with truncation errors of machine precision (see Supplementary Note 2).

**Thermal tensor network approach.** To accurately simulate the finite-temperature properties ( $T > 0$ ), in particular the thermal entropies, of the low-dimensional spin lattice models, we employ the state-of-the-art tensor network methods including the linearized tensor renormalization group (LTRG)<sup>44,45</sup> for the thermodynamics of 1D system ( $T > 0$ ), and the exponential tensor renormalization group (XTRG)<sup>46,47,78</sup> for 2D spin lattice models. Below we briefly recapitulate the finite-temperature many-body methods LTRG and XTRG.

The LTRG method can be exploited to accurately simulate the 1D HAFC model directly in the thermodynamic limit, and it has been shown very suitable for studying the universal thermodynamic in the quantum critical regime<sup>79,80</sup>. Consider the 1D HAFC described by Eq. (1) in the main text, with only NN couplings. Through the Trotter-Suzuki decomposition<sup>81</sup> the density matrix  $\rho(\beta)$  at inverse temperature  $\beta$  can be expressed as

$$\rho(\beta) = e^{-\beta H} \simeq \left( \prod_i e^{-\tau h_{2i}} e^{-\tau h_{2i+1}} \right)^n \mathcal{I}, \quad (3)$$

where  $n\tau = \beta$  and  $\mathcal{I}$  is an identity operator representing the density matrix at the infinitely high temperature. In LTRG, we regard Eq. (3) as a cooling process and contract the thermal tensor network layer by layer by projecting the imaginary-time evolution operators  $\exp(-\tau h)$  to the density operator, starting from  $\mathcal{I}$ . Once the (inverse) temperature reaches  $\beta/2$ , we use the bilayer formalism<sup>45</sup> and obtain the partition function  $Z(\beta) = \text{Tr}[\rho(\beta/2)^\dagger \rho(\beta/2)]$ , base on which we can compute the relevant thermodynamic properties, e.g., magnetic entropy  $S_m(\beta) = \ln Z - \beta \frac{\partial \ln Z(\beta)}{\partial \beta}$  with high precision.

For 2D lattice models, including the unfrustrated SLH as well as the frustrated KLH and TLH models, we employ the XTRG method<sup>46,47,78</sup> to simulate the finite-temperature properties of large-size systems and down to low temperatures. Firstly, we express the many-body Hamiltonian in a matrix product operator (MPO) form, and the high-temperature density matrix  $\rho(\tau)$  with  $\tau \ll 1$  (e.g.,  $\tau = 1 \times 10^{-4}$ ) can be obtained via a series expansion

$$\rho_\tau = e^{-\tau H} \simeq \sum_{n=0}^N \frac{(-\tau)^n}{n!} H^n, \quad (4)$$

which converges to machine precision very rapidly when retaining up to 10–20 expansion orders in practice. Given  $\rho(\tau)$ , the low-temperature density matrix  $\rho_n(\beta \equiv 2^n \tau)$  can be obtained by keeping squaring the density matrices, i.e.,

$$\rho_n(\beta) = \rho_{n-1}^\dagger(\beta/2) \cdot \rho_{n-1}(\beta/2). \quad (5)$$

Such a doubling is a natural and efficient operation for tensor networks, and XTRG approach can thus reach low-temperature many-body states as quickly as possible, i.e., exponentially, reducing the truncation iterations and thus rendering higher accuracies. With the density matrix  $\rho_n(\beta)$ , represented in thermal tensor networks as a thermofield double state, we can compute the partition function as  $Z(2\beta) = \text{Tr}[\rho_n^\dagger(\beta) \cdot \rho_n(\beta)]$ , from which various magnetothermal quantities can be computed. For example, the magnetic entropy  $S_m$  of central interest in this work can be computed via

$$S_m(\beta) = \ln Z(\beta) - \frac{\partial \ln Z(\beta)}{\partial \ln \beta}. \quad (6)$$

Since in XTRG it naturally involves the logarithmic temperature scale and thus the differential operations are preferred to be performed with respect to  $\ln \beta$ . Moreover, to collect enough data set we perform parallel XTRG calculations with interleaved temperature points so as to make sure the differentiation errors are small (see more details in refs. 46,47). In practical calculations of the quantum spin models considered in the present work, we retain up to 500 (SLH)–600 (TLH) bond states that can lead to well converged thermal data, with truncation errors  $\sim 10^{-6}$  down to 100 mK, on cylinders up to width 4 and 6 near the polarization QCP.

**Comparisons between the TLH and SLH models.** In Fig. 1, we have shown that the highly frustrated QSL models on the kagome and triangular lattices can reach much lower temperatures as compared to the unfrustrated square lattice model near the polarization field  $B_c$ . To make a more detailed comparison, in Fig. 5 we show the adiabatic cooling behaviors of the TLH system which exhibits very distinct and appealing MCE properties, as compared to that of the unfrustrated SLH model. From Fig. 5a, we see that the frustrated QSL system ( $J$ - $J'$  TLH) has a strong cooling effect not just within the vicinity of polarization field  $B_c$  but can also extend continuously to the whole regime below  $B_c$ . This is a very distinct and appealing MCE properties of the highly frustrated QSL system.

As shown in Fig. 5b, we compare the adiabatic temperature changes of the TLH and SLH systems. It is found that the TLH can reach much lower temperature than SLH in the field regime of  $B \leq B_c$ . When zoomed in into the low-temperature regime, we further see that, besides the polarization point  $B_c$ , there are certain other prominent dips in the adiabatic demagnetization curve in the TLH system (see the inset of Fig. 5b), corresponding to several quantum phase transitions. These distinct features of TLH model can be ascribed to the strong spin frustration effects: the magnetization below the polarization field has strong variations and the system undergoes several quantum phase transitions due to strongly competing spin

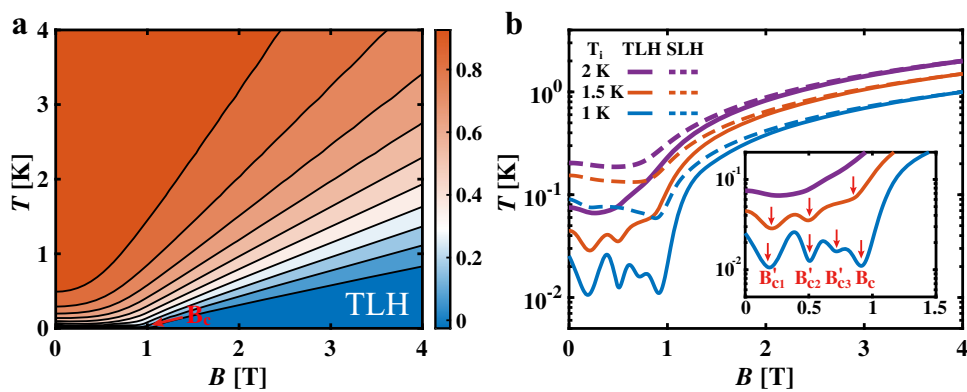


**Fig. 5 Isentropic curves of the triangular-lattice Heisenberg (TLH) and square lattice Heisenberg (SLH) models.** **a** shows the isentropic lines of the frustrated TLH model, defined on a cylinder of size  $6 \times 9$  and with couplings  $J = 0.305$  K,  $J' = 0.03$  K (i.e.,  $J'/J \simeq 0.1$ ). The temperature drops adiabatically to very low values at the polarization field of  $B_c = 1$  T and remain at low  $T$  below  $B_c$ . The color bar represents the entropy at various temperature and magnetic field. **b** compares the isentropic curves of the TLH and SLH models with various initial temperatures  $T_i = 2$  K, 1.5 K, and 1 K, with the low- $T$  regime zoomed in in the inset. At the polarization point  $B_c$ , the TLH can be cooled down to significantly lower temperature than SLH. Besides, below  $B_c$  the temperature of SLH bounces back and increases rapidly, while the TLH remains at low temperature with several dips, denoted respectively as  $B'_{c1}$ ,  $B'_{c2}$ ,  $B'_{c3}$ , and  $B_c$ , in the isentropic curves.

orders. In the main text, we restricted the discussions of MCE near the polarization field, as  $B_c$  is relatively easy to locate, and the comparisons between various models are thus more on an equal footing. Now from Fig. 5a, b, we see that the strong cooling effects enhanced by spin frustration are persistent in the low-field regime, in sharp distinction to that of the unfrustrated SLH system.

## Data availability

The data that support the findings of this study are available from the corresponding author upon reasonable request.

## Code availability

All numerical codes in this paper are available upon request to the authors.

Received: 4 March 2022; Accepted: 7 September 2022;

Published online: 21 September 2022

## References

1. Weiss, P. & Piccard, A. Le phénomène magnétocalorique. *J. Phys.* **7**, 103 (1917).
2. Debye, P. Einige Bemerkungen zur Magnetisierung bei tiefer Temperatur. *Ann. der Phys.* **386**, 1154 (1926).
3. Giauque, W. F. & MacDougall, D. P. Attainment of temperatures below 1° absolute by demagnetization of  $\text{Gd}_2(\text{SO}_4)_3 \cdot 8\text{H}_2\text{O}$ . *Phys. Rev.* **43**, 768 (1933).
4. Hagemann, C. & Richards, P. L. Adiabatic demagnetization refrigerators for small laboratory experiments and space astronomy. *Cryogenics* **35**, 303 (1995).
5. Shirron, P. et al. Development of a cryogen-free continuous ADR for the constellation-X mission. *Cryogenics* **44**, 581 (2004).
6. Shirron, P. J. Cooling capabilities of adiabatic demagnetization refrigerators. *J. Low. Temp. Phys.* **148**, 915 (2007).
7. Luchier, N. et al. 50mK cooling solution with an ADR precooled by a sorption cooler. *Cryogenics* **50**, 591 (2010).
8. Shirron, P. J. Applications of the magnetocaloric effect in single-stage, multi-stage and continuous adiabatic demagnetization refrigerators. *Cryogenics* **62**, 130 (2014).
9. Jahromi, A. E., Shirron, P. J. & DiPirro, M. J. *Sub-Kelvin Cooling Systems for Quantum Computers*, Tech. Rep. (NASA Goddard Space Flight Center Greenbelt, 2019).
10. Broholm, C. et al. Quantum spin liquids. *Science* **367**, eaay0668 (2020).
11. Zhou, Y., Kanoda, K. & Ng, T.-K. Quantum spin liquid states. *Rev. Mod. Phys.* **89**, 025003 (2017).
12. Balents, L. Spin liquids in frustrated magnets. *Nature* **464**, 199 (2010).
13. Sachdev, S. In *Quantum Phase Transitions* (ed. Sachdev, S.) 368 (Cambridge University Press, 2001).
14. Zhu, L. J., Garst, M., Rosch, A. & Si, Q. M. Universally diverging grüneisen parameter and the magnetocaloric effect close to quantum critical points. *Phys. Rev. Lett.* **91**, 066404 (2003).
15. Wolf, B. et al. Magnetocaloric effect and magnetic cooling near a field-induced quantum-critical point. *Proc. Natl Acad. Sci. USA* **108**, 6862 (2011).
16. Lang, M. et al. Magnetic cooling through quantum criticality. *J. Phys.: Conf. Ser.* **400**, 032043 (2012).
17. Lang, M. et al. Field-induced quantum criticality—application to magnetic cooling. *Phys. Status Solidi B* **250**, 457 (2013).
18. Garst, M. & Rosch, A. Sign change of the Grüneisen parameter and magnetocaloric effect near quantum critical points. *Phys. Rev. B* **72**, 205129 (2005).
19. Gegenwart, P. Grüneisen parameter studies on heavy fermion quantum criticality. *Rep. Prog. Phys.* **79**, 114502 (2016).
20. Liu, T. et al. Significant inverse magnetocaloric effect induced by quantum criticality. *Phys. Rev. Res.* **3**, 033094 (2021).
21. Zhitomirsky, M. E. Enhanced magnetocaloric effect in frustrated magnets. *Phys. Rev. B* **67**, 104421 (2003).
22. Zhitomirsky, M. E. & Honecker, A. Magnetocaloric effect in one-dimensional antiferromagnets. *J. Stat. Mech.: Theor. Exp.* **2004**, 07012 (2004).
23. Honecker, A. & Wessel, S. Magnetocaloric effect in quantum spin-s chains. *Condens. Matter Phys.* **12**, 399 (2009).
24. Sharples, J. W. et al. Quantum signatures of a molecular nanomagnet in direct magnetocaloric measurements. *Nat. Commun.* **5**, 5321 (2014).
25. Jang, D. et al. Large magnetocaloric effect and adiabatic demagnetization refrigeration with  $\text{YbPt}_2\text{Sn}$ . *Nat. Commun.* **6**, 8680 (2015).
26. Xiang, J.-S. et al. Criticality-enhanced magnetocaloric effect in quantum spin chain material copper nitrate. *Sci. Rep.* **7**, 44643 (2017).
27. Breunig, O. et al. Quantum criticality in the spin-1/2 Heisenberg chain system copper pyrazine dinitrate. *Sci. Adv.* **3**, eaao3773 (2017).
28. Tokiwa, Y. et al. Super-heavy electron material as metallic refrigerant for adiabatic demagnetization cooling. *Sci. Adv.* **2**, e1600835 (2016).
29. Tokiwa, Y. et al. Frustrated magnet for adiabatic demagnetization cooling to milli-Kelvin temperatures. *Commun. Mater.* **2**, 42 (2021).
30. Wu, L. S. et al. Tomonaga-Luttinger liquid behavior and spinon confinement in  $\text{YbAlO}_3$ . *Nat. Commun.* **10**, 698 (2019).
31. Zhong, R., Guo, S., Xu, G., Xu, Z. & Cava, R. J. Strong quantum fluctuations in a quantum spin liquid candidate with a Co-based triangular lattice. *Proc. Natl Acad. Sci. USA* **116**, 14505 (2019).
32. Li, N. et al. Possible itinerant excitations and quantum spin state transitions in the effective spin-1/2 triangular-lattice antiferromagnet  $\text{Na}_2\text{BaCo}(\text{PO}_4)_2$ . *Nat. Commun.* **11**, 4216 (2020).
33. Lee, S. et al. Temporal and field evolution of spin excitations in the disorder-free triangular antiferromagnet  $\text{Na}_2\text{BaCo}(\text{PO}_4)_2$ . *Phys. Rev. B* **103**, 024413 (2021).
34. Wellm, C. et al. Frustration enhanced by Kitaev exchange in a  $j_{\text{eff}} = \frac{1}{2}$  triangular antiferromagnet. *Phys. Rev. B* **104**, L100420 (2021).
35. Zhu, Z. & White, S. R. Spin liquid phase of the  $S = \frac{1}{2}J_1, J_2$  Heisenberg model on the triangular lattice. *Phys. Rev. B* **92**, 041105(R) (2015).

36. Iqbal, Y., Hu, W.-J., Thomale, R., Poilblanc, D. & Becca, F. Spin liquid nature in the Heisenberg  $J_1$ - $J_2$  triangular antiferromagnet. *Phys. Rev. B* **93**, 144411 (2016).
37. Gong, S.-S., Zhu, W., Zhu, J.-X., Sheng, D. N. & Yang, K. Global phase diagram and quantum spin liquids in a spin- $\frac{1}{2}$  triangular antiferromagnet. *Phys. Rev. B* **96**, 075116 (2017).
38. Hu, S., Zhu, W., Eggert, S. & He, Y.-C. Dirac spin liquid on the spin-1/2 triangular Heisenberg antiferromagnet. *Phys. Rev. Lett.* **123**, 207203 (2019).
39. Jiang, H. C., Weng, Z. Y. & Sheng, D. N. Density matrix renormalization group numerical study of the kagome antiferromagnet. *Phys. Rev. Lett.* **101**, 117203 (2008).
40. Yan, S., Huse, D. A. & White, S. R. Spin-liquid ground state of the  $S = 1/2$  Kagome Heisenberg antiferromagnet. *Science* **332**, 1173 (2011).
41. Depenbrock, S., McCulloch, I. P. & Schollwöck, U. Nature of the spin-liquid ground state of the  $S = 1/2$  Heisenberg model on the kagome lattice. *Phys. Rev. Lett.* **109**, 067201 (2012).
42. Liao, H. J. et al. Gapless spin-liquid ground state in the  $S = 1/2$  kagome antiferromagnet. *Phys. Rev. Lett.* **118**, 137202 (2017).
43. He, Y.-C., Zaletel, M. P., Oshikawa, M. & Pollmann, F. Signatures of Dirac cones in a dmrg study of the kagome Heisenberg model. *Phys. Rev. X* **7**, 031020 (2017).
44. Li, W. et al. Linearized tensor renormalization group algorithm for the calculation of thermodynamic properties of quantum lattice models. *Phys. Rev. Lett.* **106**, 127202 (2011).
45. Dong, Y. L., Chen, L., Liu, Y. J. & Li, W. Bilayer linearized tensor renormalization group approach for thermal tensor networks. *Phys. Rev. B* **95**, 144428 (2017).
46. Chen, B.-B., Chen, L., Chen, Z., Li, W. & Weichselbaum, A. Exponential thermal tensor network approach for quantum lattice models. *Phys. Rev. X* **8**, 031082 (2018).
47. Li, H. et al. Thermal tensor renormalization group simulations of square-lattice quantum spin models. *Phys. Rev. B* **100**, 045110 (2019).
48. Reis, M. S. Magnetocaloric and barocaloric effects of metal complexes for solid state cooling: review, trends and perspectives. *Coord. Chem. Rev.* **417**, 213357 (2020).
49. Wolf, B., Honecker, A., Hofstetter, W., Tutsch, U. & Lang, M. Cooling through quantum criticality and many-body effects in condensed matter and cold gases. *Int. J. Mod. Phys. B* **28**, 1430017 (2014).
50. Elstner, N., Singh, R. R. P. & Young, A. P. Finite temperature properties of the spin-1/2 Heisenberg antiferromagnet on the triangular lattice. *Phys. Rev. Lett.* **71**, 1629 (1993).
51. Elstner, N., Singh, R. R. P. & Young, A. P. Spin-1/2 Heisenberg antiferromagnet on the square and triangular lattices: a comparison of finite temperature properties. *J. Appl. Phys.* **75**, 5943 (1994).
52. Chen, L. et al. Two-temperature scales in the triangular-lattice Heisenberg antiferromagnet. *Phys. Rev. B* **99**, 140404 (2019).
53. Li, Y. et al. Gapless quantum spin liquid ground state in the two-dimensional spin-1/2 triangular antiferromagnet  $\text{YbMgGaO}_4$ . *Sci. Rep.* **5**, 16419 (2015).
54. Li, Y. et al. Muon spin relaxation evidence for the  $U(1)$  quantum spin-liquid ground state in the triangular antiferromagnet  $\text{YbMgGaO}_4$ . *Phys. Rev. Lett.* **117**, 097201 (2016).
55. Shen, Y. et al. Evidence for a spinon Fermi surface in a triangular-lattice quantum-spin-liquid candidate. *Nature* **540**, 559 (2016).
56. Paddison, J. A. M. et al. Continuous excitations of the triangular-lattice quantum spin liquid  $\text{YbMgGaO}_4$ . *Nat. Phys.* **13**, 117 (2017).
57. Cevallos, F. A., Stolze, K., Kong, T. & Cava, R. J. Anisotropic magnetic properties of the triangular plane lattice material  $\text{TmMgGaO}_4$ . *Mater. Res. Bull.* **105**, 154 (2018).
58. Shen, Y. et al. Intertwined dipolar and multipolar order in the triangular-lattice magnet  $\text{TmMgGaO}_4$ . *Nat. Commun.* **10**, 4530 (2019).
59. Li, Y. et al. Partial up-up-down order with the continuously distributed order parameter in the triangular antiferromagnet  $\text{TmMgGaO}_4$ . *Phys. Rev. X* **10**, 011007 (2020).
60. Li, H. et al. Kosterlitz-Thouless melting of magnetic order in the triangular quantum Ising material  $\text{TmMgGaO}_4$ . *Nat. Commun.* **11**, 1111 (2020).
61. Hu, Z. et al. Evidence of the Berezinskii-Kosterlitz-Thouless phase in a frustrated magnet. *Nat. Commun.* **11**, 5631 (2020).
62. Dun, Z. et al. Neutron scattering investigation of proposed Kosterlitz-Thouless transitions in the triangular-lattice Ising antiferromagnet  $\text{TmMgGaO}_4$ . *Phys. Rev. B* **103**, 064424 (2021).
63. Ranjith, K. M. et al. Anisotropic field-induced ordering in the triangular-lattice quantum spin liquid  $\text{NaYbSe}_2$ . *Phys. Rev. B* **100**, 224417 (2019).
64. Scheie, A. O. et al. Witnessing quantum criticality and entanglement in the triangular antiferromagnet  $\text{KYbSe}_2$ . Preprint at <https://arxiv.org/abs/2109.11527> (2021).
65. Xing, J., Sanjeeva, L. D., May, A. F. & Sefat, A. S. Synthesis and anisotropic magnetism in quantum spin liquid candidates  $A\text{YbSe}_2$  ( $A = \text{K}$  and  $\text{Rb}$ ). *APL Materials* **9**, 111104 (2021).
66. Liu, W. et al. Rare-earth chalcogenides: a large family of triangular lattice spin liquid candidates. *Chin. Phys. Lett.* **35**, 117501 (2018).
67. Sanders, M. B., Cevallos, F. A. & Cava, R. J. Magnetism in the  $\text{KBaRE}(\text{BO}_3)_2$  ( $\text{RE} = \text{Sm}, \text{Eu}, \text{Gd}, \text{Tb}, \text{Dy}, \text{Ho}, \text{Er}, \text{Tm}, \text{Yb}, \text{Lu}$ ) series: materials with a triangular rare earth lattice. *Mater. Res. Express* **4**, 036102 (2017).
68. Yao, W. & Li, Y. Ferrimagnetism and anisotropic phase tunability by magnetic fields in  $\text{Na}_2\text{Co}_2\text{TeO}_6$ . *Phys. Rev. B* **101**, 085120 (2020).
69. Lin, G. et al. Field-induced quantum spin disordered state in spin-1/2 honeycomb magnet  $\text{Na}_2\text{Co}_2\text{TeO}_6$ . *Nat. Commun.* **12**, 5559 (2021).
70. Zhong, R., Gao, T., Ong, N. P. & Cava, R. J. Weak-field induced nonmagnetic state in a Co-based honeycomb. *Sci. Adv.* **6**, eaay6953 (2020).
71. Dun, Z. L. et al. Magnetic ground states of the rare-earth tripod kagome lattice  $\text{Mg}_2\text{RE}_3\text{Sb}_3\text{O}_{14}$  ( $\text{Mg}_2\text{RE}_3\text{Sb}_3\text{O}_{14}$ ). *Phys. Rev. Lett.* **116**, 157201 (2016).
72. Dun, Z. et al. Quantum versus classical spin fragmentation in dipolar kagome ice  $\text{Ho}_3\text{Mg}_2\text{Sb}_3\text{O}_{14}$ . *Phys. Rev. X* **10**, 031069 (2020).
73. Liao, Y. D. et al. Phase diagram of the quantum Ising model on a triangular lattice under external field. *Phys. Rev. B* **103**, 104416 (2021).
74. Ventura, G. & Risegari, L. (eds). "7 - Other Refrigerators". in *The Art of Cryogenics* 163–171 (Elsevier, Oxford, 2008).
75. White, S. R. Density matrix formulation for quantum renormalization groups. *Phys. Rev. Lett.* **69**, 2863 (1992).
76. Schollwoeck, U. The density-matrix renormalization group in the age of matrix product states. *Annals Phys.* **326**, 96–192 (2010).
77. Östlund, S. & Rommer, S. Thermodynamic limit of density matrix renormalization. *Phys. Rev. Lett.* **75**, 3537 (1995).
78. Chen, L. et al. Two temperature scales in the triangular lattice Heisenberg antiferromagnet. *Phys. Rev. B* **99**, 140404(R) (2019).
79. Chen, L., Wang, H.-X., Wang, L. & Li, W. Conformal thermal tensor network and universal entropy on topological manifolds. *Phys. Rev. B* **96**, 174429 (2017).
80. Wang, H.-X., Chen, L., Lin, H. & Li, W. Topological and geometric universal thermodynamics in conformal field theory. *Phys. Rev. B* **97**, 220407 (2018).
81. Suzuki, M. Relationship between d-dimensional quantal spin systems and (d+1)-dimensional Ising systems equivalence, critical exponents and systematic approximants of the partition function and spin correlations. *Prog. Theor. Phys.* **56**, 1454 (1976).

## Acknowledgements

W.L. and Y.G. are indebted to Tao Liu and Yuan Wan for helpful discussions. This work was supported by the National Natural Science Foundation of China (Grant Nos. 12222412, 11834014, 11974036, 12047503, 12074023, 12074024, 12174386), Beijing Municipal Science and Technology Commission (Grant No. Z191100007219013), Strategic Priority Research Program of CAS (Grant No. XDB28000000), National Key R&D Program of China (Grant No. 2018YFA0305800), and CAS Project for Young Scientists in Basic Research (Grant Nos. YSBR-057). W.L. thanks the HPC-ITP for the technical support and generous allocation of CPU time.

## Author contributions

W.L. and G.S. initiated this work. X.Y.L., Y.G., and H.L. performed the thermal tensor network calculations and analyzed the experimental data of magnetic compounds. W.J., J.X., Z.C., and H.J. analyzed the results from the experimental point of view. All authors contributed to the preparation of the draft. G.S. and W.L. supervised the project.

## Competing interests

The authors declare no competing interests.

## Additional information

**Supplementary information** The online version contains supplementary material available at <https://doi.org/10.1038/s42005-022-01010-1>.

**Correspondence** and requests for materials should be addressed to Wei Li or Gang Su.

**Peer review information** *Communications Physics* thanks the anonymous reviewers for their contribution to the peer review of this work.

**Reprints and permission information** is available at <http://www.nature.com/reprints>

**Publisher's note** Springer Nature remains neutral with regard to jurisdictional claims in published maps and institutional affiliations.



**Open Access** This article is licensed under a Creative Commons Attribution 4.0 International License, which permits use, sharing, adaptation, distribution and reproduction in any medium or format, as long as you give appropriate credit to the original author(s) and the source, provide a link to the Creative Commons license, and indicate if changes were made. The images or other third party material in this article are included in the article's Creative Commons license, unless indicated otherwise in a credit line to the material. If material is not included in the article's Creative Commons license and your intended use is not permitted by statutory regulation or exceeds the permitted use, you will need to obtain permission directly from the copyright holder. To view a copy of this license, visit <http://creativecommons.org/licenses/by/4.0/>.

© The Author(s) 2022